Impact of Heteroatom Substitution on Dual-State Emissive Rigidified 2-(2'-hydroxyphenyl)benzazole Dyes: Towards Ultra-Bright ESIPT Fluorophores**

Thibault Pariat, Maxime Munch, Martyna Durko-maciag, Jaroslaw Mysliwiec, Pascal Retailleau, Pauline Vérité, Denis Jacquemin, Julien Massue, Gilles Ulrich

Impact of Heteroatom Substitution on Dual-State Emissive Rigidified 2-(2'-hydroxyphenyl)benzazole Dyes: Towards Ultra-Bright ESIPT Fluorophores

Thibault Pariat,[a] Maxime Munch,[a] Martyna Durko-Maciag,[a][b] Jaroslaw Mysliwiec,[b] Pascal Retailleau,[c] Pauline M. Vérité,[d] Denis Jacquemin,*[d] Julien Massue,*[a] and Gilles Ulrich*[a]

[a] Institut de Chimie et Procédés pour l'Energie, l'Environnement et la Santé (ICPEES), UMR CNRS 7515, Ecole Européenne de Chimie, Polymères et Matériaux (ECPM), 25 Rue Becquerel, 67087 Strasbourg Cedex 02, France.

[b] Advanced Materials Engineering and Modeling Group, Wroclaw University of Science and Technology, Wybrzeze Wyspianskiego 27, 50-370 Wroclaw, Poland.

[c] Laboratoire de Cristallochimie, ICSN-CNRS, 1 Avenue de la Terrasse, Bât. 27, 91198 Gif-sur-Yvette Cedex, France.

[d] CEISAM Lab-UMR 6230-CNRS and University of Nantes, Nantes, France.

Email: massue@unistra.fr, gulrich@unistra.fr, Denis.Jacquemin@univ-nantes.fr

Abstract

Dual-medium fluorophores which show significant luminescence intensity in solution and in the solid-state from two emissive forms or processes remain scarce in the literature and can only result from a subtle balance between rigidity, planarity and solubility while avoiding detrimental π-π stacking and strong molecular motions. 2-(2'-hydroxyphenyl)benzazole (HBX) fluorophores are popular Excited-State Intramolecular Proton Transfer (ESIPT) emitters largely studied for their synthetic versatility, photostability, strong solid-state fluorescence and ability to engineer dual emission paving the way to applications as white emitters, ratiometric sensors, and cryptographic dyes. They are, however heavily quenched in solution, due to efficient non-radiative pathways taking place as a consequence of the proton transfer in the excited-state. A mono- or bis-functionalization of the HBX scaffold with ethynyl-extended moieties was previously shown to yield enhanced brightness of the resulting dyes in solution. In this contribution, the nature of the heteroring constitutive of these rigidified HBX dyes was modified and we demonstrate that this simple structural modification triggers major optical changes in terms of emission color, dual emission engineering, and importantly, fluorescent quantum yield. Investigation of the photophysical properties in solution and in the solid-state of a series of ethynyl-TIPS extended HBX fluorophores, along with *ab initio* calculations demonstrate the very promising abilities of these dyes to act as bright dual-state emitters, in both solution (even in protic environments) and solid-state.

Introduction

The molecular engineering of functional fluorescent dyes with enhanced optical properties is of upmost importance for the large panel of cutting-edge applications targeted by these systems, including organic light-emitting diodes (OLEDs), super-resolution microscopy or solid-state lasers.[1] Excited-State Intramolecular Proton Transfer (ESIPT) luminescence is typically observed on heterocycles presenting an intramolecular hydrogen bond forming five-, six- or seven-membered rings.[2] This optical process relies on a photoinduced proton transfer in the excited-state resulting in the characteristic red-shifted emission of a tautomeric (T^*) species. As a consequence, ESIPT emission is characterized by a strong spectral separation between absorption and emission bands, generally accompanied by an optical profile highly sensitive to the surrounding microenvironment.[3] An intense emission in the solid-state is also a trademark of ESIPT dyes, since, unlike the majority of organic fluorophores undergoing aggregation-caused quenching (ACQ), they strongly brighten up in the solid-state owing to a beneficial restriction of intramolecular motions in the excited-state facilitated by the proton transfer.[4] Additionally, it is possible to partially frustrate the ESIPT process with appropriate electronic substitution resulting in dual emission from the two excited tautomers.[5] A complete frustration of ESIPT is also possible *via* extended π-conjugation at strategic positions, leading to very emissive push-pull dyes.[6] All these features open unique perspectives for the engineering of smart luminescent materials, capable of modulating their optical properties in different environments or upon external stimulation. Notably, recent ESIPT-based molecular systems capable of reversible mechanochromism,[7] aggregation-induced emission (AIE),[8] ratiometric sensing,[9] white-light emission,[10] anti-counterfeiting[11] as well as multiple applications based on single dye have been reported.[12] The ESIPT process is now well-documented and has been unraveled in structurally-diverse dyes over the years, with a variety of H-bond donors and acceptors and an emphasis on modifying the heterocycle that carries the proton transfer site.[13] For all these probes, a similar challenge is faced, *i.e.*, addressing the lack of strong emission intensity in dilute solution due to efficient deexcitation routes. One of the key desexcitation processes is related to an easily reachable conical intersection corresponding to the twisting between the two moieties after proton transfer. Such accessible intersection largely impeded the use of ESIPT dyes outside constrained matrixes.[14] A key factor to engineer solution-state emissive ESIPT dyes while keeping strong solid-state emission is clearly molecular rigidity. Indeed, recent rigidified scaffolds based on imidazo[1,2-f]phenanthridine,[15] 2,5-dithienylpyrrole[16] among others[17] showed promising dual

(solution/solid) state emission (DSE), a highly desirable feature among fluorescent dyes allowing expanding the range of applications.[18] Recent examples reported the wide structural variety of DSE dyes and demonstrated their use in many applications.[19] Nevertheless, a subtle equilibrium between planarity, rigidity and solubility has to be maintained during the design of ESIPT-based DSE probes, as planar, rigidified dyes are usually prone to detrimental π-π stacking in solution, leading to insolubility and fluorescence quenching. In short, combining the attractive properties of ESIPT luminescence with the actual applications targeted by DSE dyes remains one desirable objective of the field. The groups involved in the present investigation have recently tackled this challenge by using 2-(2'-hydroxyphenyl)benzoxazole (HBO) model fluorophores, owing to their synthetic availability, finely tunable photophysical properties, and facile dual emission engineering. The simple incorporation of rigid ethynyl-extended moieties at the periphery of the H-bond donor (phenol ring) afforded a strong enhancement of the luminescence intensity in solution, both in protic and aprotic media as compared to unsubstituted references (Figure 1a).[20] These dyes showed promising ability to act as random lasers in doped polymers, paving the way to the use of these dyes as DSE probes with an enlarged scope of applications.[21] In parallel with the development of our rigidified probes, several studies hinted that substituted 2-(2'-hydroxyphenyl)benzimidazole (HBI) dyes present significantly larger fluorescence quantum yields in solution, as compared to their oxygen or sulfur analogs, by reducing non-radiative desexcitations in the excited-state.[22] Switching to HBI dyes can therefore be seen as an attractive alternative to engineer HBX-based DSE dyes without introducing additional aromatic ring and inherent solubility issues.

In this article, we combine these two beneficial effects: 1) the introduction of ethynyl-extended silyl substituents at the periphery of the molecular scaffold, and 2) the presence of benzimidazole core in lieu of benzoxazole and benzothiazole (Figure 1b). We demonstrate that these unprecedented cooperative effects lead to the ESIPT-based probes that are highly emissive in both solution and solid-state. These dyes were fully characterized structurally and optically and a strong contribution of the nature of the heteroatom was evidenced. The results are additionally rationalized with first-principle calculations.

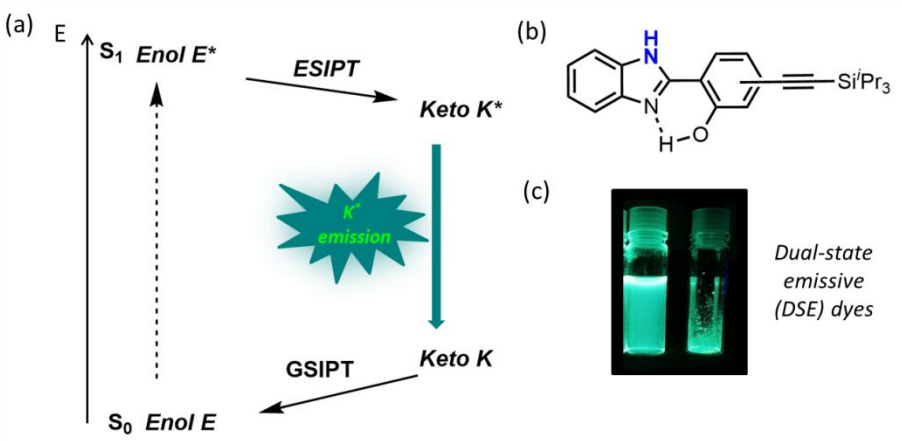

Figure 1. (a) Enol-keto phototautomerism at the origin of ESIPT emission (b) Structure of the HBI dyes studied and (c) Representative photo of HBI **8** in toluene solution and powder under irradiation (λ_{exc} =365 nm).

Synthesis

The preparation of HBI dyes **5-8** is described on Scheme 1. The target HBI dyes were prepared from commercially available salicylaldehydes **A-D** in two steps. The first step involves a Pd-catalyzed Sonogashira cross-coupling reaction to provide the corresponding bis-(triisopropylsilyl)acetylene extended salicylaldehydes **1-4** in 25-97% yield. Intermediates **1-4** were then converted in HBI dyes **5-8** by bubbling O_2 in the presence of a slight excess of 1,2-benzenediamine and sodium metabisulfite followed by microwave heating at 120°C.

HBO dyes **9-12** and HBT **13** were also prepared as reference compounds (Figure 2, see the SI for synthetic protocols). All compounds were characterized by ^{1}H, ^{13}C NMR spectroscopy along with high resolution mass spectrometry (HR-MS).

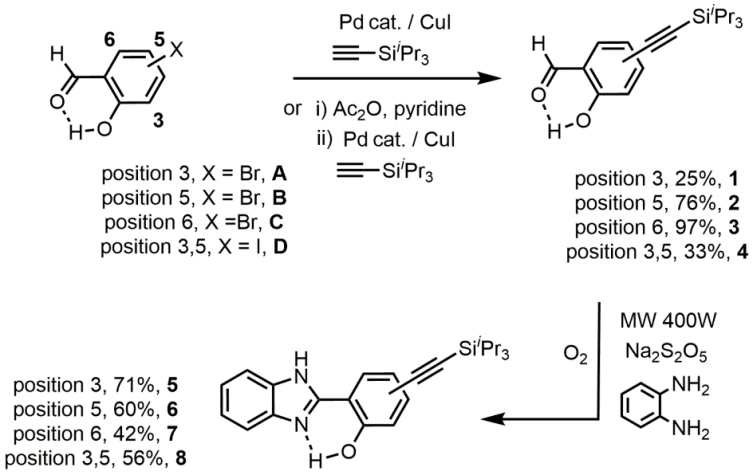

Scheme 1. Synthesis of HBI dyes **5-8**.

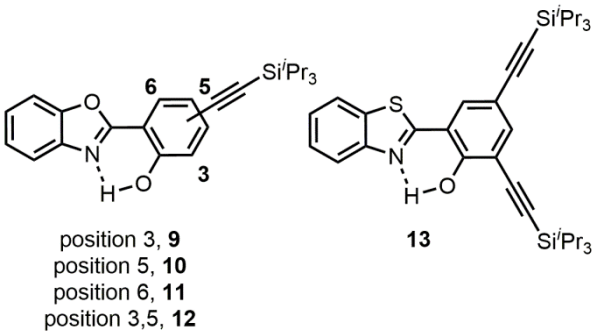

Figure 2. HBO dyes **9-12** and HBT dye **13**.

Experimental section

Materials and methods

All chemicals were received from commercial sources (SigmaAldrich, Fluorochem) and used without further purification. Tetrahydrofuran (THF) was distilled over metallic sodium (Na). Dichloromethane (DCM) was distilled over P_2O_5 under an argon atmosphere. Triethylamine (Et_3N) was distilled under argon over KOH. Thin layer chromatography (TLC) was performed on silica gel coated with fluorescent indicator. Chromatographic purifications were conducted using 40-63 μm silica gel. All mixtures of solvents are given in v/v ratio. ^{1}H NMR (500 or 400 MHz) and ^{13}C NMR (125 or 100 MHz) spectra were recorded on a Bruker Advance 500 or 400 MHz spectrometers with perdeuterated solvents with residual protonated solvent signals as internal references. Absorption spectra were recorded using a dual-beam grating Schimadzu UV-3000 absorption spectrometer with a quartz cell of 1 cm of optical path length. The steady-state fluorescence emission and excitation spectra were obtained by using a Horiba Jobin Yvon Fluoromax 4. All fluorescence and excitation spectra were corrected. Solvents for spectroscopy were spectroscopic grade and were used as received.

The fluorescence quantum yields (Φ_{exp}) were measured in diluted solution with an absorption value below 0.1 at the excitation wavelength using equation 1:

$$\Phi_{exp} = \Phi_{ref} \frac{I}{I_{ref}} \frac{OD_{ref}}{OD} \frac{\eta^2}{\eta^2_{ref}} \quad (eq\ 1)$$

I is the integral of the corrected emission spectrum, OD is the optical density at the excitation wavelength, and η is the refractive index of the medium. The reference systems used were: Quinine Φ = 55% in H_2SO_4 1N (λ_{exc} = 366 nm) for dyes emitting below 480 nm, Rhodamine 6G, Φ = 88% in ethanol (λ_{exc} = 488 nm) for dyes emitting between 480 and 570 nm and cresyl violet, Φ = 55% (λ_{exc} = 546 nm) in ethanol for dyes emitting above 570 nm.

Luminescence lifetimes were measured on an Edinburgh Instruments spectrofluorimeter equipped with a R928 photomultiplier and a PicoQuant PDL 800-D pulsed diode connected to a GwInstect GFG- 8015G delay generator. No filter was used for the excitation. Emission wavelengths were selected by a monochromator. Lifetimes were deconvoluted with FS-900 software using a light-scattering solution (LUDOX) for instrument response. The excitation source was a laser diode (λ_{exc} = 320 nm).

General procedure for salicylaldehyde 1 and 4: To a solution of halogeno-hydroxybenzaldehyde **A** or **D** (1.5 mmol) in dichloromethane (20 mL) was added pyridine (1.5 mmol) and acetic anhydride (30 mmol). The resulting mixture was stirred at room temperature three hours before it was quenched with a saturated solution of $NaHCO_3$ 1M. It was then extracted with dichloromethane, washed with water three times, dried over $MgSO_4$, and concentrated *in vacuo* to afford the corresponding acetate-protected salicylaldehyde which was used without further purification. The obtained compound was dissolved in toluene (20 mL) and triethylamine (5 mL) before $Pd(dppf)Cl_2$ (0.15 mmol) was added. The resulting suspension was degassed with argon for 30 minutes before (triisopropylsilyl)acetylene (4.5 mmol) and CuI (0.3 mmol) were added. The medium was stirred at 90°C overnight. The crude solution was then taken up in dichloromethane, washed with water, dried over $MgSO_4$, and concentrated *in vacuo*. The crude residue was purified by silica gel chromatography (petroleum ether/dichloromethane) to afford 2-hydroxy-3-((triisopropylsilyl)ethynyl) benzaldehyde **1** or 2-hydroxy-3,5-(bis-(triisopropylsilyl)ethynyl) benzaldehyde **4** as pale yellow solids.

Salicylaldehyde 1: 25%. ^{1}H NMR (500 MHz, $CDCl_3$) δ = 11.35 (s, 1H), 9.89 (s, 1H), 7.67 (dd, J = 7.5, 1.7 Hz, 1H), 7.52 (dd, J = 7.7, 1.7 Hz, 1H), 6.97 (t, J = 7.7 Hz, 1H), 1.15 (m, 21H). ^{13}C NMR (126 MHz, $CDCl_3$) δ = 196.2, 162.8, 140.6, 133.7, 120.7, 119.6, 113.6, 100.7, 97.6, 18.8, 11.4. ESI-HRMS: calcd for $C_{18}H_{27}O_2Si$: 303.1775 (M+H), found 303.1779 (M+H).

Salicyaldehyde 4: 33%. ^{1}H NMR (500 MHz, $CDCl_3$) δ = 11.43 (s, 1H), 9.86 (s, 1H), 7.73 (d, J = 2.1 Hz, 1H), 7.64 (d, J = 2.1 Hz, 1H), 1.17 – 1.11 (m, 42H). ^{13}C NMR (126 MHz, $CDCl_3$)

δ = 195.7, 162.5, 143.1, 137.1, 120.4, 115.5, 114.1, 104.5, 99.8, 98.4, 90.8, 18.8, 18.8, 11.4. ESI-HRMS: calcd for $C_{29}H_{47}O_2Si_2$: 483.3109 (M+H), found 483.3089 (M+H).

General procedure for salicylaldehyde 2 and 3: To a solution of bromo-hydroxy benzaldehyde **B or C** (1.5 mmol) in toluene (20 mL) and triethylamine (5 mL), Pd(dppf)Cl_2 (0.15 mmol) was added. The resulting suspension was degassed with argon for 30 minutes before (triisopropylsilyl)acetylene (4.5 mmol) and CuI (0.3 mmol) were added. The medium was stirred at 90°C overnight. The crude solution was then taken up in dichloromethane, washed with water, dried over $MgSO_4$, and concentrated *in vacuo*. The crude residue was purified by silica gel chromatography (petroleum ether/dichloromethane) to afford 2-hydroxy-5-((triisopropylsilyl)ethynyl) benzaldehyde **2** or 2-hydroxy-6-((triisopropylsilyl)ethynyl) benzaldehyde **3** as pale yellow solids.

Salicyaldehyde 2: 76%. ^{1}H NMR (500 MHz, $CDCl_3$) δ = 11.10 (s, 1H), 9.87 (d, J = 0.6 Hz, 1H), 7.70 (d, J = 2.1 Hz, 1H), 7.61 (dd, J = 8.7, 2.1 Hz, 1H), 6.94 (d, J = 8.6 Hz, 1H), 1.13 (s, 21H). ^{13}C NMR (126 MHz, $CDCl_3$) δ = 196.3, 161.6, 140.5, 137.5, 120.5, 118.1, 115.7, 105.3, 90.4, 18.8, 11.5. ESI-HRMS: calcd for $C_{18}H_{27}O_2Si$: 303.1775 (M+H), found 303.1765 (M+H).

Salicyaldehyde 3: 97%. ^{1}H NMR (500 MHz, $CDCl_3$) δ = 11.65 (s, 1H), 10.51 (s, 1H), 7.43 (dd, J = 8.5, 7.5 Hz, 1H), 7.11 (dd, J = 7.5, 1.1 Hz, 1H), 6.94 (d, J = 8.4 Hz, 1H), 1.16 – 1.11 (m, 21H). ^{13}C NMR (126 MHz, $CDCl_3$) δ = 197.1, 162.5, 136.7, 127.8, 125.9, 119.9, 118.5, 101.7, 99.5, 18.8, 11.4. ESI-HRMS: calcd for $C_{18}H_{27}O_2Si$: 303.1775 (M+H), found 303.1769 (M+H).

General procedure for HBI dyes 5-8: To a solution of salicylaldehyde **1-5** (1 mmol) in DMF (20 mL), 1,2-benzenediamine (1.1 mmol) and sodium metabisulfite (1.1 mmol) were added in a multi-mode microwave reactor. The resulting mixture was degassed with O_2 for 15 minutes and then heated by microwaved irradiation (400 W) for 30 minutes at 120 °C. After cooling down, the reaction medium was taken up in ethylacetate, washed with brine, dried over $MgSO_4$, and concentrated *in vacuo*. The crude residue was purified by silica gel chromatography (petroleum ether/dichloromethane) and the purified compound was recrystallized in a mixture dichloromethane/ethanol to afford HBI dyes **5-8** as a yellow solids.

HBI 5: 71%. ^{1}H NMR (500 MHz, $CDCl_3$) δ = 12.64 (s, 1H), 9.94 (s, 1H), 7.67 (dd, J = 7.9, 1.6 Hz, 1H), 7.61 (s, 2H), 7.51 (dd, J = 7.6, 1.5 Hz, 1H), 7.33 – 7.27 (m, 2H), 6.89 (t, J = 7.7 Hz, 1H), 1.18 (s, 21H). ^{13}C NMR (126 MHz, $CDCl_3$) δ = 159.8, 150.8, 135.7, 125.3, 123.6, 118.9, 113.4, 112.8, 102.3, 96.7, 18.9, 11.5. ESI-HRMS: calcd for $C_{24}H_{31}N_2OSi$: 391.2200 (M+H), found 391.2180 (M+H).

HBI 6: 60%. ^{1}H NMR (500 MHz, $CDCl_3$) δ = 13.31 (s, 1H), 9.53 (s, 1H), 7.74 (s, 1H), 7.63 (m, 2H), 7.48 (d, J = 8.5 Hz, 1H), 7.33 (dd, J = 6.1, 3.1 Hz, 2H), 7.07 (d, J = 8.6 Hz, 1H), 1.15 (s, 21H). ^{13}C NMR (126 MHz, $CDCl_3$) δ = 159.3, 150.6, 135.9, 128.3, 123.8, 118.4, 114.4, 112.2, 106.5, 89.3, 18.9, 11.5. ESI-HRMS: calcd for $C_{24}H_{31}N_2OSi$: 391.2200 (M+H), found 391.2175 (M+H).

HBI 7. 42%. ^{1}H NMR (500 MHz, $CDCl_3$) δ = 14.29 (s, 1H), 11.90 (s, 1H), 7.72 – 7.50 (m, 2H), 7.36 – 7.31 (m, 2H), 7.28 (t, J = 7.9 Hz, 1H), 7.19 – 7.15 (m, 2H), 1.26 – 1.22 (m, 21H). ^{13}C NMR (126 MHz, $CDCl_3$) δ = 160.2, 151.2, 130.7, 125.9, 123.7, 119.5, 119.4, 112.4, 108.4, 98.2, 18.9, 11.6. ESI-HRMS: calcd for $C_{24}H_{31}N_2OSi$: 391.2200 (M+H), found 391.2213 (M+H).

HBI 8. 56%. ^{1}H NMR (400 MHz, $CDCl_3$) δ = 7.75 (d, J = 2.0 Hz, 1H), 7.69 – 7.61 (m, 2H), 7.60 (d, J = 2.0 Hz, 1H), 7.36 – 7.30 (m, 2H), 1.18 (s, 21H), 1.15 (s, 21H). ^{13}C NMR (126 MHz, $CDCl_3$) δ = 160.0, 150.1, 138.8, 128.8, 123.9, 114.3, 113.8, 112.7, 105.6, 101.5, 97.2, 89.7, 18.9, 18.8, 11.5, 11.5. ESI-HRMS: calcd for $C_{35}H_{51}N_2OSi_2$: 571.3534 (M+H), found 571.3519 (M+H).

X-Ray diffraction

Single crystals of HBI **6-8** and HBO **12** were obtained by slow evaporation of dichloromethane/ethanol solutions. For all dyes, X-ray diffraction analyses reveal an essentially co-planar arrangement between the phenol and the benzazole cycle, which is strongly structured by the intramolecular H-bond between the phenolic proton and the nitrogen atom of the heterocycle (Figures 3-4). Deviation from planarity, as evidenced by a twist or modification of the dihedral angle seems to depend on the number and position of the elongated and bulky ethynyl-TIPS groups on the phenolic core. Planarity seems to be reinforced when the phenolic scaffold is doubly symmetrically substituted at the 3 and 5 positions, as in HBI **8**. This planarity may also be favored by the presence of an ethanol molecule doubly involved in intermolecular H-bonds as acceptor of the NH group of HBI **8** in the asymmetric unit and donor to the OH phenolic group. In the case a mono ethynyl-TIPS substitution in position 5 of the phenol ring, as in HBI **7**, the twist reaches its highest amplitude which remains rather limited (*ca* 7.7° of plane deviation) but is half reduced if the monosubstitution lies at the 5 position (HBI **6**), where the ethynyl-TIPS moiety flanks the main core of the molecule. The relatively high twist observed in the doubly 3,5-disubstituted HBO **12** (*ca* 7° of plane deviation) contrasting with its benzimidazole analogue HBI **8** might

be due to the molecule disorder both at the level of a TIPS group and the flipped aromatic core (see the SI). It may be also due to the longest intramolecular H-bond distance observed in HBO **12**, *min* 2.641(9) *vs* 2.549(2)Å in HBI **8** (Table S2). Indeed, if the C–O (from the benzoxazole) and C–NH (from the benzimidazole) bond distances are similar, the double C=N bond shared in both compounds, appears shorter in the case of the benzoxazole in HBO **12** implying a slightly distended intramolecular interaction (see the SI).

With respect to the crystal assembling, both HBI **8** and HBO **12** crystallize in the same space group, *P*-1, with similar unit cell dimensions, reflecting the head-to-tail molecular pairing and the π-π stacking interaction propagating along the **a** direction between the inversion related main cores (Figure 5). These quasi-planar platforms parallel to the (7 -6 6) plane present regular separation of 3.47Å in HBI **8**, with the shortest centroid (phenol)-centroid(imidazole) distance of 3.6 Å. This pairing is further stabilized in HBI **8** by two ethanol molecules clamping it on both sides. In contrast, the spacing between adjacent platforms in HBO **12** alternates from 3.32 to 3.46 Å, probably in relation with the alternate flip disorder. The 3D-framework structure is building as a staircase along the ***b*** direction. In HBI **6**, which crystallizes in a much higher symmetry space group, the orthorhombic *P bca* group, the molecules related by the glide plane perpendicular to **c** with **a**/2 glide component also stacked head-to-tail with a main core rotation relative to each other of *ca* 30° and shortest centroid-centroid distance of 3.69Å between imidazole groups (Figure 6). N–H···O intermolecular H-bonds between the molecules related by the glide plane perpendicular to ***a*** with ***b***/2 translation develop corrugated sheets along the ***b*** direction (Figure 7 and Table S1). In HBI **7**, whose crystal belongs to the monoclinic space group I2/a, molecules alternatively stack head-to-head and head-to-tail along the ***a*** direction with respective spacing of *ca* 3.8 and *ca* 3.5Å (Figure 8).

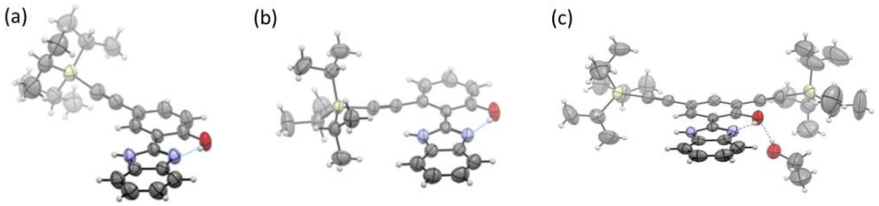

Figure 3. ORTEP views of (a) HBI **6**, (b) HBI **7** and (c) HBI **8**. Displacement ellipsoids are drawn at the 50% probability level and hydrogen atoms with an arbitrary radius size. Cyan dashed lines underscore the intramolecular hydrogen bond, O-H…N.

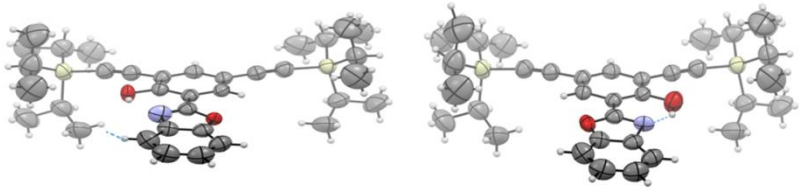

Figure 4. ORTEP views of HBO **12** showing the central core flip but not the substituent disorder. Displacement ellipsoids are drawn at the 50% probability level and hydrogen atoms with an arbitrary radius size. Cyan dashed lines underscore the intramolecular hydrogen bond, O-H…N.

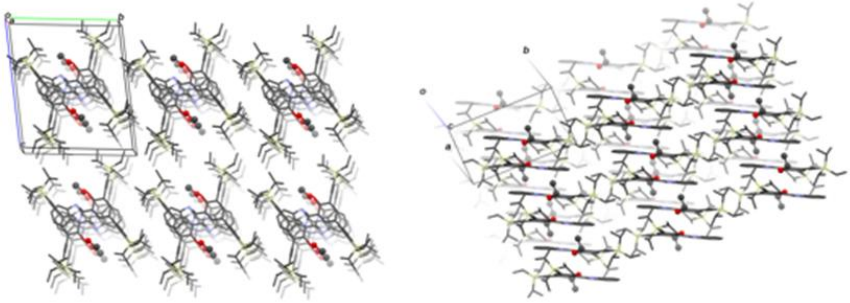

Figure 5. Crystal packing of HBI **8**, (left) viewed down the ***a*** axis, showing the head-to-tail stacking; (right) showing the staircase formation along the ***b*** direction.

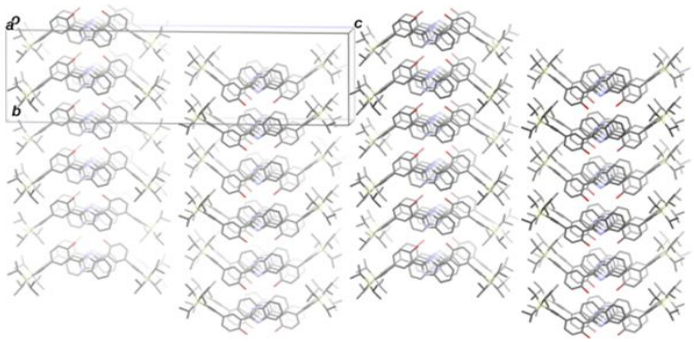

Figure 6. Crystal packing of HBI **6** down the ***a*** axis, showing the head-to-tail molecular stacking.

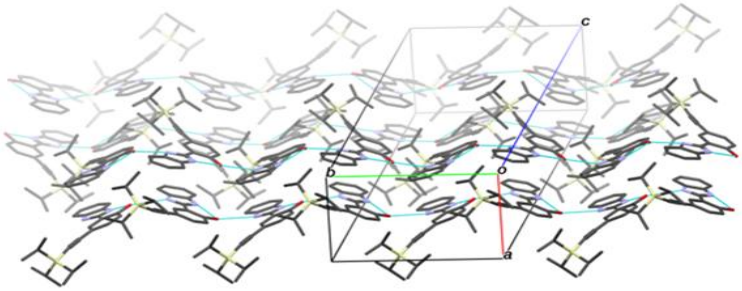

Figure 7. Partial view of the crystal packing of HBO **12** showing the corrugated sheet formation by intermolecular H-bonds (cyan dashed lines) running along the ***b*** axis.

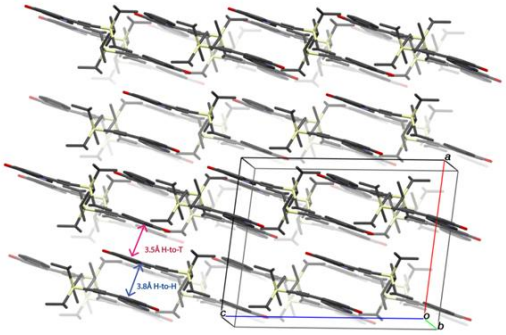

Figure 8. Crystal packing of **HBI 7** viewed down the ***a*** axis (left); down the ***b*** axis (right).

Photophysical properties

The photophysical properties of HBX dyes **5-13** have been studied in solution in solvents of different polarities as well as in the solid-state, as embedded in potassium bromide (KBr) pellets. The photophysical data are listed in Table 1.

Table 1. Photophysical data for HBX dyes **5-13** recorded in aerated solutions of various solvents at 25°C and in the solid-state.

Dye	λ_{abs} (nm)	ε ($M^{-1}.cm^{-1}$)	λ_{em} (nm)	ΔS[b] (cm^{-1})	Φ_F [c]	τ[d] (ns)	K_r[e] ($10^8 s^{-1}$)	K_{nr}[e] ($10^8 s^{-1}$)	Solvent
HBI **5**	353	21000	496	8600	0.51	4.5	1.1	1.1	Toluene
HBI **5**	348	21000	481	7900	0.53	4.5	1.2	1.0	EtOH
HBI **5**	349[a]		470	7400	0.36				KBr
HBI **6**	347	16000	482	8100	0.54	4.6	1.2	1.0	Toluene
HBI **6**	342	16000	466	7800	0.54	4.6	1.2	1.0	EtOH
HBI **6**	347[a]		460	7100	0.39				KBr
HBI **7**	346	18000	479	8000	0.49	4.7	1.0	1.1	Toluene
HBI **7**	342	15000	470	8200	0.39	5.0	0.8	1.2	EtOH
HBI **7**	332[a]		488	9600	0.68				KBr
HBI **8**	368	17000	507	7500	0.53	4.9	1.1	1.0	Toluene
HBI **8**	365	17500	492	7100	0.58	5.0	1.2	0.9	EtOH
HBI **8**	366	18000	498	7200	0.45	4.6	1.0	1.2	THF
HBI **8**	364/420	15600	447/486	1400	0.27	4.5	0.6	1.6	ACN
HBI **8**	367/428	35000	449	1100	0.57	4.1	1.4	1.0	DMF
HBI **8**	367[a]		490	6800	0.30				KBr
HBO **9**	340	15500	536	10800	0.24	3.1	0.8	2.5	Toluene
HBO **9**	337	17000	443/525	7100	0.14	2.3	0.6	3.8	EtOH
HBO **9**	335[a]		536	11200	0.51				KBr
HBO**10**	338	12000	518	10000	0.11	3.9	0.3	2.3	Toluene
HBO**10**	335	13400	403/505	5000	0.04	4.3	0.1	2.2	EtOH
HBO**10**	339[a]		504	9700	0.58				KBr
HBO**11**	322	22000	515	6600	0.15	4.6	0.3	1.9	Toluene
HBO**11**	319	20000	404/508	11500	0.04	4.2	0.1	2.3	EtOH
HBO**11**	371[a]		496	6800	0.49				KBr
HBO**12**	371	14000	535	8300	0.32	3.8	0.8	1.7	Toluene

HBO**12**	368	12500	526	8200	0.31	3.0	1.0	2.3	EtOH
HBO**12**	369	13500	527	8100	0.20	3.5	0.6	2.3	THF
HBO**12**	365	12500	525	8300	0.26	3.6	0.7	2.0	ACN
HBO**12**	368/454	8000	480	1200	0.32	4.4	0.7	1.6	DMF
HBO**12**	372[a]		530	8000	0.82				KBr
HBT**13**	378	13000	572	9000	0.15	2.5	0.6	3.5	Toluene
HBT**13**	378/425	11500	490/582	3100	0.07	3.0	0.2	3.1	EtOH
HBT**13**	376	14000	575	9200	0.07	1.3	0.5	7.3	THF
HBT**13**	374/454	11000	487/556	1500	0.03	3.8	0.1	2.5	ACN
HBT**13**	462	33000	488	1200	0.20	2.1	1.0	1.0	DMF
HBT**13**	331		574	12800	0.48				KBr

[a] Excitation wavelength, [b] Stokes' shift, [c] Relative quantum yield determined in solution using Rhodamine 6G as a reference (λ_{exc} = 488 nm, Φ = 0.88 in ethanol) or absolute quantum yield determined in films using an integration sphere, [d] Fluorescence lifetimes recorded upon excitation at 350 nm, [e] k_r (10^8 s^{-1}) and k_{nr} (10^8 s^{-1}) were calculated using: $k_r = \Phi_F/\sigma$, $k_{nr} = (1- \Phi_F)/\sigma$ where σ is the lifetime.

The absorption spectra in toluene for HBI dyes **5-8** and HBX **9-13** are presented on Figures 9a and 9b respectively while their emission spectra can be found on Figures 10a and 10b, respectively.

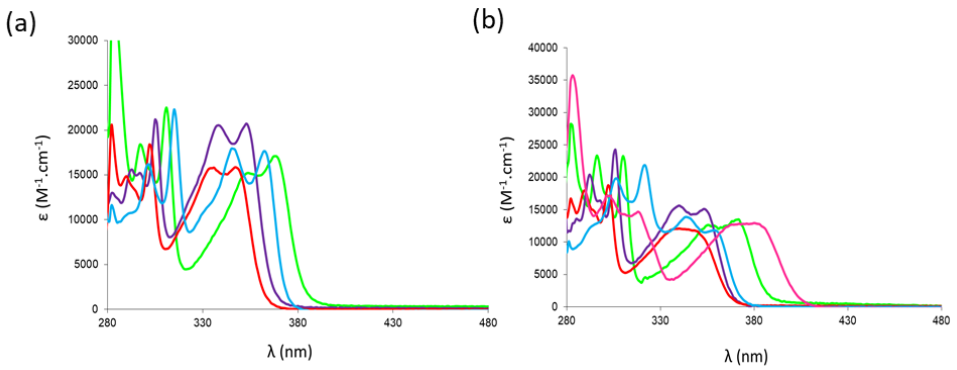

Figure 9. UV-Vis. spectra of (a) HBI **5** (purple), **6** (red), **7** (blue), **8** (green) and (b) HBO **9** (purple), **10** (red), **11** (blue), **12** (green) and HBT **13** (pink) in toluene.

HBI dyes **5-8** display absorption profiles usually observed for related dyes, *i.e.*, a main weakly structured absorption band, corresponding to the S_0-S_1 transition. The number and the position of the ethynyl-TIPS substitution have very little impact on the absorption wavelength or the molar absorption coefficient (λ_{abs} = 346-368 nm with ε = 16000-21000 $M^{-1}.cm^{-1}$ for **5-8**). Additional absorption bands are observed below 300 nm which can be assigned to π-π^* transitions of the various conjugated moieties of the dyes. In their oxygen or sulfur analogs (HBX **9-13**) more significant differences between mono- and bis-functionalized dyes are found in terms of maximum absorption wavelength (λ_{abs} = 322-340 nm for HBO **9-11** *vs.* λ_{abs} = 371 nm for HBO **12** and λ_{abs} = 378 nm for HBT **13**). Similar trends are observed in ethanol

(λ_{abs} = 348, 342, 342, 365, 337, 335, 319, 368, 378 nm for HBX **5-13**, respectively) (Figures S5.27 and S5.28).

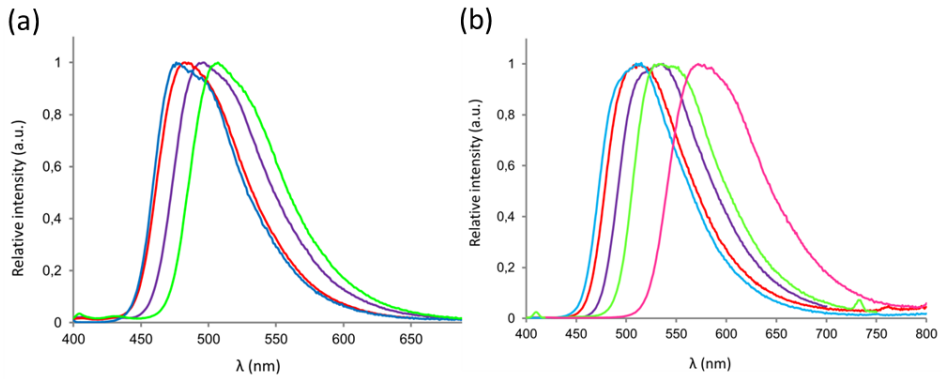

Figure 10. Fluorescence spectra of (a) HBI **5** (purple), **6** (red), **7** (blue), **8** (green) and (b) HBO **9** (purple), **10** (red), **11** (blue), **12** (green) and HBT **13** (pink) in toluene (λ_{exc} = 320-370 nm).

In toluene, photoexcitation on the lowest-energy absorption band leads to the observation of an intense single emission band centered at 496, 482, 479 and 507 nm for HBI **5-8**, respectively. This band, which is strongly spectrally separated from the corresponding absorption band (Stokes' shift in the range 7500-8600 cm^{-1}) is attributed to the sole decay of the excited K^* tautomer, as a result of a quantitative ESIPT process. This assignment is confirmed by the theoretical calculations (*vide infra*). The influence of the position of the ethynyl-TIPS functionalization on the emission wavelength seems to be mild. Nevertheless, substitution in position 3, as in HBI dyes **5** and **8** seems to induce a bathochromic shift, both in absorption and emission as compared to positions 5 or 6, as in **6** and **7** (λ_{abs}/ λ_{em} = 353/496 nm and 368/507 nm for **5** and **8** respectively *vs*. λ_{abs}/ λ_{em} = 347/482 nm and 346/479 nm for **6** and **7**, respectively). This mild effect is reproduced theoretically as well (*vide infra*). In ethanol, the maximum emission wavelengths are similar as those observed in toluene (λ_{em} = 460-492 nm), indicating that the K^* tautomer is very mildly sensitive to the nature of the solvent, *i.e.*, not very polar (Figure S5.29). Protic solvents are typically reported to stabilize the E^* state *via* intermolecular H-bonds, leading to a partial frustration of the ESIPT process. Nevertheless, and quite surprisingly, no dual E^*/K^* emission is observed in ethanol for HBI **5-8**, as a presumable strong influence of the electron donating nitrogen atom leading to enhanced basicity of the benzazole ring in the excited-state. The emission of HBO **9-12** are all significantly red-shifted as compared to their nitrogenous analogs HBI **5-8** and the fluorescence takes place in the green-yellow region, *i.e.* their maximum emission wavelength in toluene range from 515 to 536 nm.

Again, a discrimination is observed between HBO dyes **9**, **12** and **10**, **11** (λ_{em} = 535-536 nm *vs*. 515-518 nm), highlighting position 3 of the phenol as a key position to obtain bathochromic shifts, irrespective of the nature of the heteroring. In ethanol, a typical dual E^*/K^* emission is observed as a result of intermolecular stabilizations in protic solvents, except for HBO dye **12** where the K^* band is only observed. The E^* band is always characterized by a rather weak intensity as compared to the K^* band (see the SI) and a smaller Stokes' shift than the K^* band, consistent with the absence of the ESIPT process leading to a significantly smaller reorganization of the π-conjugated core in the excited-state. The maximum emission wavelength of the E^* band is bathochromically shifted to a greater extent that the K^* one, highlighting a stronger polarity of the first excited-state; a feature already observed on related HBX probes (figure S5.30).[5a]

In toluene or ethanol, HBT **13** displays an intense yellow-orange emission which is strongly red-shifted as compared to their analogs HBI **8** and HBO **12** (λ_{em} = 572 nm and 490/582 nm in toluene and ethanol respectively, see Figures 11 and S5.30). The nature of the heteroatom in the series of HBX dyes studied clearly impacts significantly the emission wavelength with a ranking: λ_{em} HBI < λ_{em} HBO < λ_{em} HBT (for a similar substitution), the changes induced by the position of the substituent(s) on the aromatic core being comparatively smaller. Moreover, a marked effect on the stabilization of the first excited-state E^* is also observed in ethanol.

To shed more light on the optical properties of these HBX dyes, the absorption and emission spectra of HBX **8**, **12** and **13**, all displaying a double ethynyl-TIPS substitution have been recorded in a range of solvents with different physical properties (toluene, ethanol, THF, acetonitrile and DMF) (Table 1 and Figure 11).

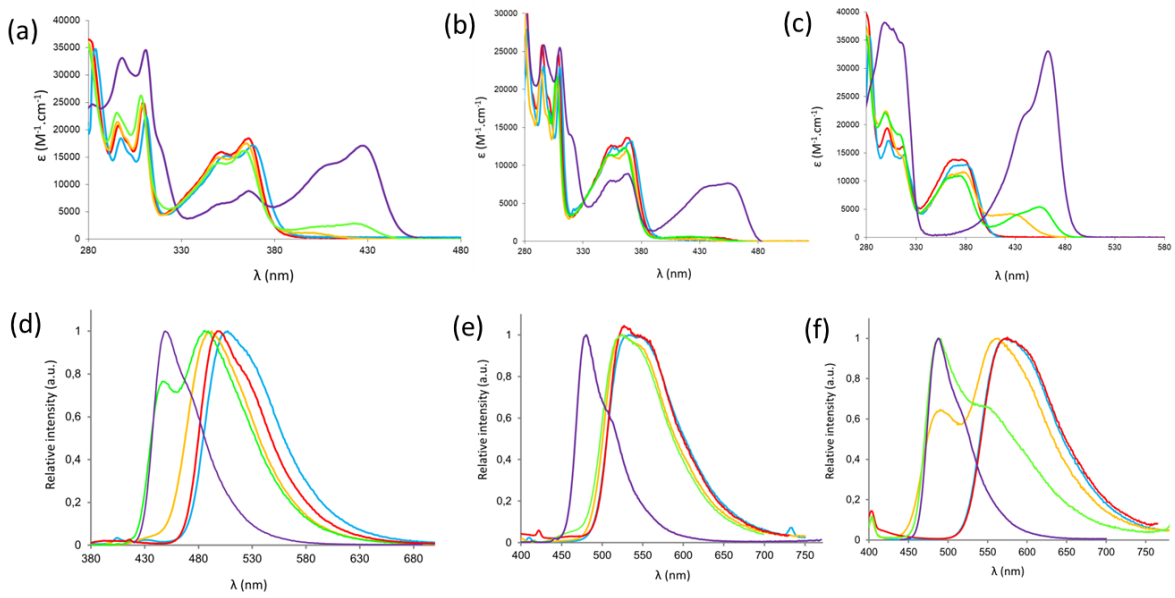

Figure 11. UV-Vis. Spectra in toluene (blue), ethanol (orange), THF (red), acetonitrile (green) and DMF (purple) of (a) HBI **8**, (b) HBO **12** and (c) HBT **13** and fluorescence spectra in toluene (blue), ethanol (orange), THF (red), acetonitrile (green) and DMF (purple) of (d) HBI **8**, (e) HBO **12** and (f) HBT **13**.

In absorption, regardless of the solvent, the three HBX dyes display similar features, *i.e.*, a main band corresponding to the S_0-S_1 transition whose maximum does not vary significantly. However, in acetonitrile, a weakly intense red-shifted band can be observed in the case of HBI **8** and HBT **13** (λ_{abs} = 420 nm and 454 nm for **8** and **13**, respectively). We underline that this band is absent in the case of HBO **12**, but can also be observed in ethanol for HBT **13** only (λ_{abs} = 425 nm), evidencing the intimate relationship between the heteroatom and the solvatochromism. In DMF, the intensity of this band does increase regardless of the heteroatom, but to different extents depending on the nature of the heterocycle: for HBT **13**, this band is the only one observable (λ_{abs} = 462 nm) whereas for HBI **8** and HBO **13**, it does coexist with the S_0-S_1 transition found in other solvents (λ_{abs} = 367 and 368 nm, respectively). This absorption band is assigned to the presence of the stabilized anionic species D, corresponding to the deprotonation of the phenol in dissociative solvents. The stabilization of this charged species in the ground state is reminiscent to other reported examples[10e, 23] and can be rationalized by the presence of a small π-conjugation at the para position of the phenolate (position 5), beneficial for the stability of the corresponding conjugated base. Upon excitation in the main absorption band, in all solvents outside DMF, an intense emission band is

observed for all HBX dyes, whose maximum wavelength does not strongly vary in the series for a given heteroatom, indicative of the K^* nature of the emissive structure. However, it is noteworthy that the fluorescence emission is systematically red-shifted when one does switch the heteroatom from nitrogen to oxygen, and next to sulfur, going from green emission for HBI **8** (λ_{em} = 486-507 nm), to yellow emission for HBO **12** (λ_{em} = 525-535 nm) to yellow-orange for HBT **13** (λ_{em} = 556-582 nm) (Figure 12). This observation further highlights the strong influence of the nature of the dye on the stabilization of the excited-state.

Although a single band is observed in toluene and THF, in acetonitrile, a dual D^*/K^* emission is recorded for HBI **8** and HBT **13** (λ_{em} = 447/486 nm and 487/556 nm, respectively) whereas only the K^* band can be seen for HBO **12** (λ_{em} = 525 nm). In DMF, the sole presence of the D^* band is observed when excitation takes place in the lowest-energy absorption band (λ_{em} = 449, 480 and 488 nm for **8**, **12** and **13**, respectively). This observation is consistent with the well-known enhanced acidity of the phenolic proton in the excited-state in ESIPT dyes. In protic ethanol, only HBT **13** displays a dual emission whose first band's emission wavelength is similar to that observed in DMF (λ_{em} = 490 nm *vs*. 488 nm for **13** in ethanol and DMF, respectively). The similar position as in DMF along with a corresponding red-shifted absorption band clearly hints that D^* band is the main hypothesis for this higher energy excited-state in ethanol.

The most striking features of these HBX dyes **5-13** lie in the values of the quantum yields recorded in solution (Table 1). As expected, the introduction of a benzimidazole heteroring is highly beneficial to reduce non-radiative desexcitations which translates into unprecedented quantum yields in solution for HBI **5-8**, spanning 39-58% in the range of solvents studied. These values are among the highest found in the literature for rigidified single ESIPT emitters, paving the way to applications requiring strong brightness. We stress that the increase of the dielectric constant of the solvent does not drastically modify the fluorescence intensity. HBI **8** displays a quantum yield of 58% in protic ethanol, highlighting the minimal effect of intermolecular interactions on the fluorescence intensity.

The evolution of the quantum yields of HBX **8**, **12** and **13** in the different solvents studied is represented on Figure 12a while photographs under UV light are shown on Figure 12b.

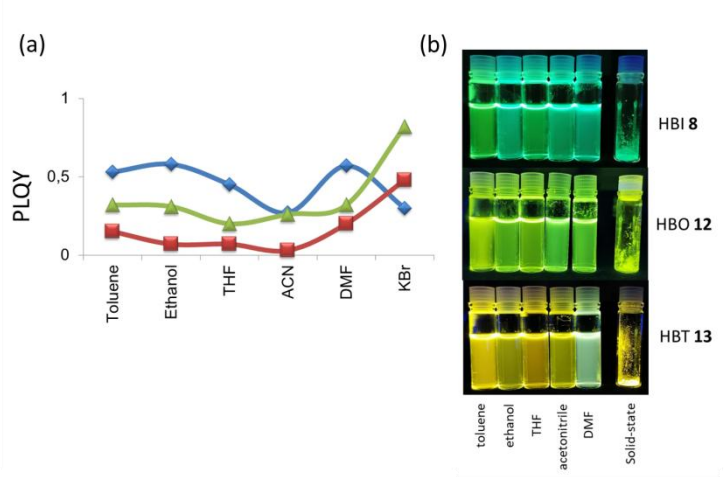

Figure 12. (a) Comparison of PLQY values in different solvents for HBI **8** (blue), HBO **12** (green) and HBT **13** (red) and (b) Photographs under irradiation (λ_{exc} = 365 nm) of HBI **8** (top), HBO **12** (middle) and HBT **13** (bottom) in solution and the solid-state.

In all solvents, HBI dyes **5-8** are significantly more fluorescent than their oxygen or sulfur counterparts HBX **9-13**. These values are especially higher than those recorded for unsubstituted HBX analogs (table S5.1), evidencing a beneficial effect of combining the presence of a benzimidazole ring and ethynyl-TIPS substituents. HBO **12** displays quantum yields in the range 26-32%, while HBT **13** is the least fluorescent dye in the series (Φ = 3-15%). These lower values for HBT **13** can be explained by strong non-radiative desexcitations constants (k_{nr}) which are consistent with reported examples and with a small barrier to the conical intersection as compared to HBO and HBI analogs (see the calculations below).[5a] In addition, HBT derivatives are known to be able to more easily form triplet states due to a sizeable intersystem crossing process at room temperature, further enhancing k_{nr} values of the emission.[24]

In DMF, where the ESIPT is frustrated due to a competitive deprotonation, large quantum yields are also recorded for all disubstituted dyes (Φ = 20-57%), consistent with a lesser reorganization of the molecular scaffold in the excited-state, once a phenolate is formed. Again, the deprotonated form of HBI **8** is the brightest in the series, highlighting again the beneficial influence of this scaffold.

Fluorescent lifetimes are all very short with monoexponential decays, in the nanosecond range (all below 2 ns) which are typical values for organic fluorophores.

In order to further investigate the formation of the anionic species observed in the course of our experiments, in the ground- and excited-state, basic titrations in absorption and emission

were performed on HBI **8**, HBO **12** and HBT **13** upon addition of increasing equivalents of a tetramethylammonium hydroxide (Me_4NOH) in acetonitrile (Figure 13).

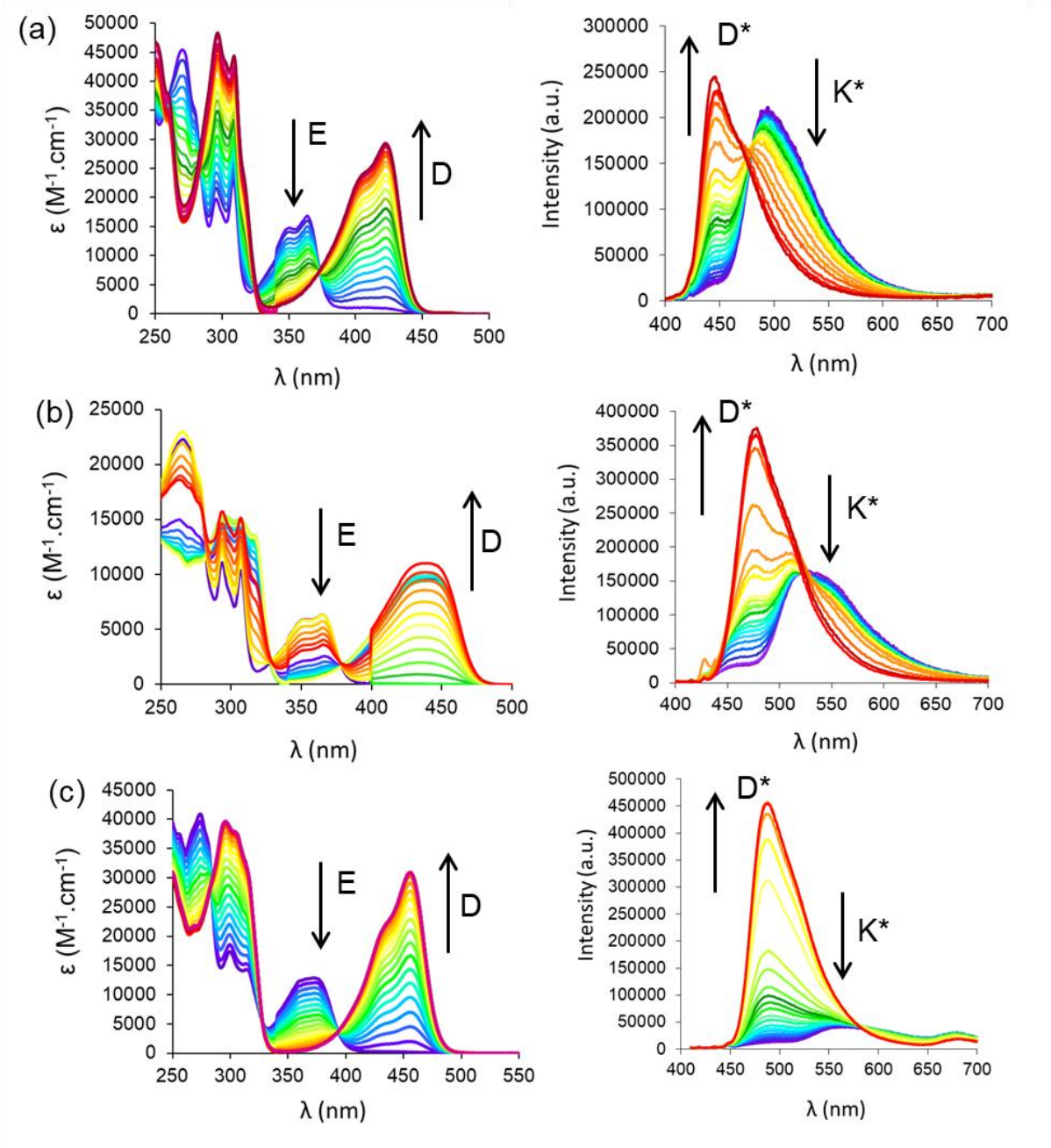

Figure 13. Superposition of absorption (left) and emission (right) spectra of (a) HBI dye **8**, (b) HBO **12**, and (c) HBT **13** in acetonitrile recorded after successive addition of increasing equivalents of Me_4NOH.

For all dyes, in absorption, the addition of increasing amounts of base leads to a progressive decrease of intensity of the band around 365 nm corresponding to the $S_0 \rightarrow S_1$ transition (E band). Concomitantly a strong increase of the band centered on 420 nm is also observed. This

band can be unambiguously ascribed to the *in situ* formation of the anionic species D, stabilized by the small electronic delocalization at the para position of the phenol ring. Three isobestic points can be identified in the course of the titration (λ_{abs} = 373, 380 and 394 nm for HBI **8**, HBO **12** and HBT **13**, respectively). Photoexcitation at these isobestic points in the presence of increasing equivalents of base triggers a decrease of the intensity of the K^* band to the benefice of the formation *in situ* of the D^* band. After addition of three equivalents of base, the intensity of the D^* band does reach a plateau, corresponding to the full deprotonation of HBX dyes **8**, **12**, and **13** which does not evolve up to six equivalents. The emission wavelength of the D* band observed during this titration does match those recoded in DMF, evidencing the instant formation of the anionic species in this dissociative solvent in the ground or excited-state. Plotting the ratio of intensity of D^*/K^* *vs.* the number of base equivalents gives a good correlation in each case (figure S5.31).

HBX dyes **5-13** appeared to be very bright powders under irradiation at 365 nm under UV (Figure 13) which evidenced their DSE properties. Their photophysical behavior in the solid-state as dispersed in potassium bromide pellets was studied (figure 14).

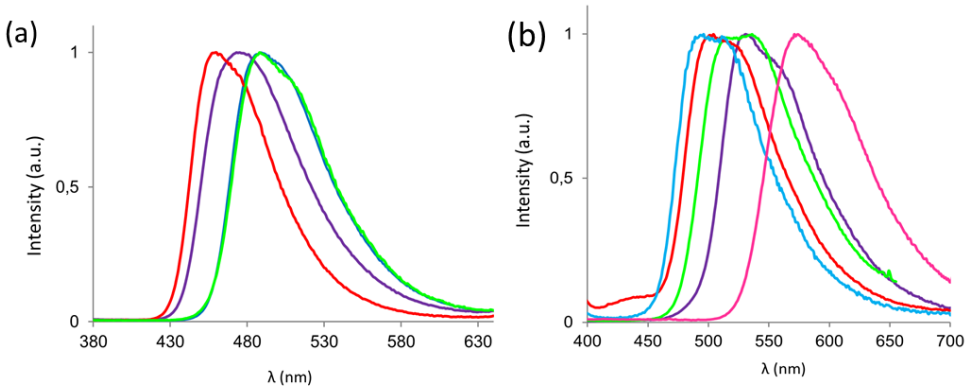

Figure 14. Fluorescence spectra of (a) HBI **5** (purple), **6** (red), **7** (blue), **8** (green) and (b) HBO **9** (purple), **10** (red), **11** (blue), **12** (green) and HBT **13** (pink) in the solid-state as dispersed in KBr pellets (λ_{exc} = 320-370 nm) (concentration around 10^{-6} M).

The emission profiles of HBX **5-13** in the solid-state appeared to be very similar to those observed in toluene, *i.e.*, a single K^* emission band ranging from 488-574 nm depending mostly on the nature of the heteroring rather than the position of the ethynyl-TIPS substitution. Photoluminescent quantum yields, calculated by integration sphere, are in the range 30-68% for HBI **5-8**, 49-82% for HBO **9-12** and 48% for HBT **13**.

First-principle calculations

Figures 15 and S7.1 show theoretical analyses with electron density difference (EDD) plots. Such representations provide a qualitative representation and show favorable conditions for the ESIPT process to occur. The changes of density are well marked on both the hydroxy group which does lose density in the excited state and the nitrogen atom which in contrast gains electronic density upon photoexcitation. Although these general features are common to all compounds studied (Figure S7.1), an interesting impact of the substitution position is also found with these plots, *i.e.* the ethynyl linkers always act a donor groups (*i.e.* losing density in S_1), a feature expected when located at the 6 position (HBX dyes **7** and **11**). One can also notice that the donor effect of the triple bond is stronger in position 5 (*para*) than 3 (*ortho*), a statement holding for both mono- and disubstituted dyes. In contrast, no major qualitative change is noticed when modifying the heteroatom.

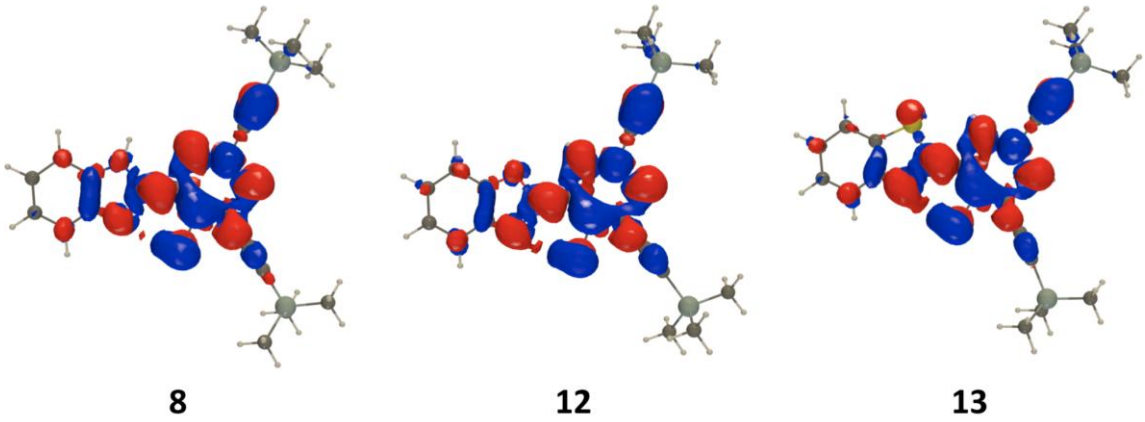

Figure 15. Representation of the density difference between the S_1 and S_0 states for **8**, **12**, and **13**. Blue and red lobes correspond to decrease and enhancement of the electronic density upon excitation, respectively. Contour value: 0.0008.

The vertical emission energies from both the E^* and K^* forms were computed for all compounds. All minimizations yield to very bright states (large oscillator strengths), indicating that there is no quenching by a low-lying dark state, consistent with the experimental observations of a large brightness for all HBX derivatives. Irrespective of the selected level of theory (TD-DFT with or without additional corrections, see Table S2), the E^* is found to emit in the 3-3.6 eV (ca. 360 nm) domain, whereas the K^* tautomer should fluoresce in the 2.2-2.6 eV (ca. 500 nm) domain. The mean absolute deviation (MAD) between the CC2-corrected values and the experimental emission maxima is clearly smaller for K^* (0.12 eV) than E^* (0.88 eV). Although such comparisons between vertical theoretical

values and experimental λ_{fl} neglect vibronic couplings, the assignment of the experimental emission to the tautomer K^* is clearly confirmed by such comparison.

In addition, the experimental trends are nicely reproduced by theoretical calculations. Indeed, for HBX dyes **8**, **12** and **13** which display the same structure but differ by their heteroatom only, HBT **13** is the most red-shifted (2.17/2.24 eV experimentally/theoretically), and HBI **8** the most blue-shifted (2.44/2.49 eV), HBO **12** being intermediate (2.32/2.44 eV).

From Figure 15, it is quite clear that this effect is not related to the different nature of the excited state but rather to the direct influence of the heteroatom, *e.g.* the more delocalizable nature of the electronic cloud of sulfur in the case of HBT **13**. Interestingly, for the keto forms of HBX dyes **8**, **12** and **13**, theory returns a drop of the dipole moment in going from the ground to the excited state (-3.21, -3.75 and -4.27 D for HBX **8**, **12**, and **13** respectively), consistent with the small negative solvatochromism observed for that band experimentally (Table 1). As for the HBI **5-8** series, which allows to study the impact of the position of substitution for a fixed heteroatom, the qualitative agreement between theory and experiment is again excellent with the same ranking of the emission energy (HBI **6** (2.57/2.62 eV) ≈ HBI **7** (2.59/2.64 eV) > HBI **5** (2.50/2.55 eV), and HBI **8** (2.44/2.49 eV).

In Table 2, the excited-state energy differences obtained for several processes in toluene are presented (see Figure S7.2 for a qualitative representation of the potential energy surface), where the $E^* \rightarrow K^*$ value gives the relative energy of the keto and enol tautomer (a negative value indicating a driving force for the ESIPT process), the $E^* \rightarrow$ TS-PT* value corresponds to the forward ESIPT barrier, and the $K^* \rightarrow$ TS-TW* value corresponds to the barrier separating the keto form from the conical intersection related to a 90° twisting around the bond connecting the two subunits of the dye, which is known to be a key deactivation pathway. First, for the former, strong ESIPT driving forces are obtained; the K^* tautomer being more stable than the corresponding E^* one by at least 0.16 eV, indicative of quantitative ESIPT,[5b] consistent with the experimental observation in toluene. Second, the computed ESIPT barriers are all negative except for HBI **7** (in which it is only very slightly positive), which is due to the consideration of ZPVE effects in the calculations (the barriers are all positive when ZPVE are neglected), clearly hinting that the proton transfer is barrierless (nearly barrierless in the case of HBI **7**). Finally, and more interestingly, the barriers protecting the K^* from the non-radiative twisting deexcitation are significantly dependent on the nature of the heteroatom. In the HBI series, theory returns barriers values of 0.36 eV, indicating that the interring twisting cannot be easily reached and that the keto tautomer is

stable, consistent with large fluorescence quantum yields. For the HBO dyes **9-12**, the barriers values are in the 0.23-0.29 eV range, that remains sizeable but are nevertheless smaller, hinting that this deactivation path can be activated. Finally, the barrier drops significantly for HBT **13** (0.15 eV), so that the deactivation pathway is the most efficient in the HBX series. It is interesting to note that for the HBX series **8, 12** and **13**, the computed $K^* \rightarrow$ TS-TW^* barrier heights are roughly proportional to the observed quantum yields.

Table 2. Computed TD-DFT/LR+cLR relative energies (E+ZPVE, in eV) for various processes in the excited-state of the different dyes (see text). In three cases, the twisting transition state could not be located by our calculations.

Dye	$E^* \rightarrow K^*$	$E^* \rightarrow$ TS-PT^*[a]	$K^* \rightarrow$ TS-TW^*[b]
HBI **5**	-0.34	-0.06	n.f.
HBI **6**	-0.32	-0.05	n.f.
HBI **7**	-0.16	+0.06	0.36
HBI **8**	-0.42	-0.07	0.36
HBO **9**	-0.27	-0.04	0.29
HBO **10**	-0.22	-0.03	0.23
HBO **11**	-0.17	-0.04	n.f.
HBO **12**	-0.22	-0.01	0.27
HBT **13**	-0.32	-0.04	0.15

[a] Associated transition state-proton transfer (TS-PT), [b] Associated transition state-twisted conformation (TS-TW)

Conclusion

In conclusion, a whole series of HBX derivatives mono- or bis-functionalized with ethynyl-TIPS substituents at various positions have been synthesized and characterized structurally and spectroscopically. Variation of the nature of the heteroring (benzoxazole, benzothiazole or benzimidazole) revealed a strong influence of the heteroatom, in terms of emission wavelength, stabilization of the first excited-state and most importantly quantum yields values. The beneficial presence of a benzimidazole ring in the HBI series leads to the observation of unprecedented enhanced fluorescence intensity in solution, even in protic environment, while maintaining strong emission in the solid-state. These dyes thus appear as promising dual state emissive (DSE) fluorophores. The insertion of the optimized rigidified HBI dyes in devices in currently under investigation in our laboratory.

Acknowledgments

The authors thank the CNRS and the ANR for support in the framework of the GeDeMi grant. P.M.V. and D.J. thank the CCIPL (Centre de Calcul Intensif des Pays de la Loire) installed in Nantes for generous allocation of computational time.

References

(1) (a) Y. Watanabe, H. Sasabe, J. Kido, *Bull. Chem. Soc. Jpn*. **2019**, 92, 716-728. (b) L. Wang, M.S. Frei, A. Salim, K. Johnsson, *J. Am. Chem. Soc*., **2019**, 161, 2770-2781. (c) M.K. Bera, P. Pal, S. Malik, *J. Mater. Chem. C*, **2020**, 8, 788-802.

(2) (a) C.-L. Chen, Y.-T. Chen, A.P. Demchenko, P.-T. Chou, *Nat. Rev. Chem*., **2018**, 2, 7, 131-143. (b) J. Massue, D. Jacquemin, G. Ulrich, *Chem. Lett*., **2018**, 47, 9, 1083-1089.

(3) (a) J. Zhao, S. Ji, Y. Chen, H. Guo, P. Yang, *Phys. Chem. Chem. Phys*. **2012**, 14, 8803-8817. (b) V.R. Mishra, C.W. Ghanavatkar, N. Sekar, *ChemistrySelect*, **2020**, 5, 2103-2113.

(4) (a) V.S. Padalkar, S. Seki, *Chem. Soc. Rev*. **2016**, 45, 169-202. (b) H. Wu, S. Wang, J. Ding, R. Wang, Y. Zhang, *Dyes and Pigments*, **2020**, 182, 108665.

(5) (a) E. Heyer, K. Benelhadj, S. Budzák, D. Jacquemin, J. Massue, G. Ulrich, *Chem. Eur. J*. **2017**, 23, 7324-7336. (b) C. Azarias, S. Budzák, A.D. Laurent, G. Ulrich, D. Jacquemin, *Chem. Sci*. **2016**, 7, 3763-3774. (c) E. Heyer, J. Massue, G. Ulrich, *Dyes and Pigments*, **2017**, 143, 18-24. (d) H.-Q.Yin, F. Yin, X.-B. Yin, *Chem. Sci*., **2019**, 10, 11103-11109.

(6) (a) M. Raoui, J. Massue, C. Azarias, D. Jacquemin, G. Ulrich, *Chem. Commun*. **2016**, 52, 9216-9219. (b) B. Li, G. Tang, L. Zhou, D. Wu, J. Lan, L. Zhou, Z. Lu, J. You, *Adv. Funct. Mater*., **2017**, 27, 1605245.

(7) (a) Y.C. Wei, Z. Zhang, Y.-A. Chen, C.-H. Wu, Z.-Y. Liu, S.-Y. Ho, J.-C. Liu, J.-A. Lin, P.-T. Chou, *Comm. Chem*., **2019**, 2, 1, 1-9. (b) E. Horak, M. Robic, A. Simanovic, V. Mandic, R. Vianello, M. Hranjec, I. Murkovic Steinberg, *Dyes and Pigments*, **2019**, 162, 688-696.

(8) (a) S. Biswas, R. Mengji, S. Barman, V. Venugopal, A. Jana, N.D.P. Singh, *Chem. Commun*., **2018**, 54, 168-171. (b) Q. Feng, Y. Li, L. Wang, C. Li, J. Wang, Y. Liu, K. Li, H. Hou, *Chem. Commun*., **2016**, 52, 3123-3126. (c) K. Li, Q. Feng, G. Niu, W. Zhang, Y. Li, M. Kang, K. Xu, J. He, H. Hou, B.Z. Tang, *ACS Sens*., **2018**, 3, 920-928.

(9) (a) A.C. Sedgwick, L. Wu, H.-H. Han, S.D. Bull, X.-P. He, T.D. James, J.L. Sessler, B.Z. Tang, H. Tian, J. Yoon, *Chem. Soc. Rev*., **2018**, 47, 8842-8880. (b) P. Saravana Kumar, P. Raja Lakshmi, K.P. Elango, *New J. Chem*., **2019**, 43, 675-680. (c) S. Sinha, B. Chowdhury, P. Ghosh, *Inorg. Chem*., **2016**, 55, 9212-9220.

(10) (a) S. Park, J.E. Kwon, S.H. Kim, J. Seo, K. Chung, S.-Y. Park, D.-J. Jang, B.M. Medina, J. Gierschner, S.Y. Park, *J. Am. Chem. Soc*. **2009**, 131, 14043-14049; (b) K.-C. Tang, M.-J. Chang, T.-Y. Lin, H.-A. Pan, T.-C. Fang, K.-Y. Chen, W.-Y. Hung, Y.-H. Hsu, P.-T. Chou, *J. Am. Chem. Soc*. **2011**, 133, 17738-17745. (c) K. Benelhadj, W. Muzuzu, J. Massue, P. Retailleau, A. Charaf-Eddin, A.D. Laurent, D. Jacquemin, G. Ulrich, R. Ziessel, *Chem. Eur. J*., **2014**, 20, 12843-12857. (d) B. Li, J. Lan, D. Wu, J. You, *Angew. Chem., Int. Ed*., **2015**, 54, 14008-14012. (e) K.-I. Sakai, T. Ishikawa, T. Akutagawa, *J. Mater. Chem. C*, **2013**, 1, 7866-7871.

(11) Y. Zhang, H. Yang, H. Ma, G. Bian, Q. Zang, J. Sun, C. Zhang, Z. An, W.-Y. Wang, *Angew. Chem., Int. Ed*., **2019**, 58, 8773-8778.

(12) S. Sinha, B. Chowdhury, U.K. Ghorai, P. Ghosh, *Chem. Commun*., **2019**, 55, 5127-5130.

(13) (a) T. Mutai, T. Muramatsu, I. Yoshikawa, H. Houjou, M. Ogura, *Org. Lett*., **2019**, 21, 2143-2146. (b) M. Zhang, R. Cheng, J. Lan, H. Zhang, L. Yan, X. Pu, Z. Huang, D. Wu, J. You, *Org. Lett*., **2019**, 21, 4058-4062. (c) H.-W. Tseng, T.-C. Lin, C.-L. Chen, T.-C. Lin, Y.-A. Chen, J.-Q. Liu, C.-H. Hung, C.-M. Chao, K.-M. Liu, P.-T. Chou, *Chem. Commun*., **2015**, 51, 16099-16102. (d) H. Liu, X. Cheng, H. Zhang, Y. Wang, H. Zhang, S. Yamaguchi, S. *Chem. Commun*. **2017**, 53, 7832-7835.

(14) (a) Z.R. Grabowski, K. Rotkiewicz, W. Rettig, *Chem. Rev*., **2003**, 103, 3899-4032. (b) A. Maliakal, G. Lem, N.J. Turro, R. Ravichandran, J.C. Suhadolwik, A.D. DeBellis, M.G. Wood, J. Lau, *J. Phys. Chem. A*, **2002**, 106, 7680-7689. (c) A.P. Demchenko, K.-C. Tang, P.-T. Chou, *Chem. Soc. Rev*., **2013**, 42, 1379-1408.

(15) K. Skonieczny, J. Yoo, J.M. Larsen, E.M. Espinoza, M. Barbasiewicz, V.I. Vullev, C.-H. Lee, D.-T. Gryko, *Chem. Eur. J*. **2016**, 22, 7485-7496.

(16) (a) N. Suzuki, A. Fukazawa, K. Nagura, S. Saito, H. Kitoh-Nishioka, S. Irle, D. Yokogawa, S. Yamaguchi, *Angew. Chem., Int. Ed*., **2014**, 53, 8231-8235. (b) N. Suzuki, K. Suda, D. Yokogawa, H. Kitoh-Nishioka, S. Irle, A. Ando, L.M.G. Abegão, K. Kamada, A. Fukazawa, S. Yamaguchi, Chem. Sci., **2018**, 9, 2666-2673.

(17) (a) K. Takagi, K. Ito, Y. Yamada, T. Nakashima, R. Fukuda, M. Ehara, H. Masu, *J. Org. Chem.* **2017**, 82, 12173-12180. (b) Y.-H. Hsu, Y.-A. Chen, H.-W. Tseng, Z. Zhang, J.-Y. Shen, W.-T. Chuang, T.-C. Lin, C.-S. Lee, B.-C. Hong, S.-H. Liu, P.-T. Chou, *J. Am. Chem. Soc*., **2014**, 136, 11805-11812.

(18) (a) H. Wu, Z. Chen, W. Chi, B.A. Kaur, L. Gu, C. Qian, B. Wu, B. Yue, G. Liu, G. Yang, L. Zhu, Y. Zhao, *Angew. Chem., Int. Ed*., **2019**, 58, 33, 11419-11423. (b) A. Goel, A. Sharma, M. Rawat, R.S. Anand, R. Kant, *J. Org. Chem*. **2014**, 79, 10873-10880. (c) A. Raghuvanshi, A.K. Jha, A. Sharma, S. Umar, S. Mishra, R. Kant, A. Goel, *Chem. Eur. J*. **2017**, 23, 4527-4531. (d) Q. Qiu, P. Xu, Y. Zhu, J. Yu, M. Wei, W. Xi, H. feng, J. Chen, Z. Qian, *Chem. Eur. J*., **2019**, 25, 15983-15987.

(19) (a) Y. Xu, L. Ren, D. Dang, Y. Zhi, X. Wang, L. Meng, *Chem. Eur. J*. **2018**, 24, 10383-10389. (b) M. Huang, J. Zhou, K. Xu, X. Zhu, Y. Wan, *Dyes and Pigments*, **2019**, 160, 839-847. (c) X. Zhang, Y. Zhou, M. Wang, Y. Chen, Y. Zhou, W. Gao, M. Liu, X. Huang, H. Wu, *Chem. Asian. J*.

2020, 15, 1692-1700. (d) D. Göbel, D. Duvinage, T. Stauch, B.J. Nachtsheim, *J. Mater. Chem. C*, **2020**, 8, 9213-9225. (e) G. Xia, Q. Shao, K. Liang, Y. Wang, L. Jiang, H. Wang, *J. Mater. Chem. C*, **2020**, 8, 13621-13626.

(20) (a) J. Massue, A. Felouat, M. Curtil, P.M. Vérité, D. Jacquemin, G. Ulrich, *Dyes and Pigments*, **2019**, 160, 915-922. (b) J. Massue, G. Ulrich, R. Ziessel, *Eur. J. Org. Chem.*, **2013**, 5701-5709.

(21) (a) J. Massue, A. Felouat, P.M. Vérité, M. Curtil, D. Jacquemin, K. Cyprych, M. Durko, L. Sznitko, J. Mysliwiec, G. Ulrich, *Phys. Chem. Chem. Phys*., **2018**, 20, 19958-19963. (b) J. Massue, T. Pariat, P. M. Vérité, D. Jacquemin, M. Durko, T. Chtouki, L. Sznitko, J. Mysliwiec, G. Ulrich, *Nanomaterials*, **2019**, 9, 1093.

(22) (a) S.R Vasquez, M.C. Rodriguez, M. Mosquera, F. Rodriguez-Prieto, *J. Phys. Chem. A*, **2008**, 112, 376-387. (b) T. Iijima, A. Momotake, Y. Shinohara, T. Sato, Y. Nishimura, T. Arai, *J. Phys. Chem. A*, **2010**, 114, 1603-1609. (c) S.K. Behera, G. Sadhuragiri, P. Elumalai, M. Sathiyendiran, G. Krishnamoorthy, *RSC Adv.*, **2016**, 6, 59708-59717. (d) N. Manojai, R. Daengngern, K. Kerdpol, C. Ngaojampa, N. Kungwan, *J. Luminescence*., **2017**, 188, 275-282.

(23) (a) M. Munch, M. Curtil, P.M Vérité, D. Jacquemin, J. Massue, G. Ulrich, *Eur. J. Org. Chem*., **2019**, 1134-1144. (b) J. Cheng, D. Liu, L. Bao, K. Xu, Y. Yang, K. Han, *Chem. Asian J*., **2014**, 9, 3215-3220.

(24) (a) Q. Wang, L. Xu, Y. Niu, Y. Wang, M.-S. Yuan, Y. Zhang, *Chem. Asian J*., **2016**, 11, 3454-3463. (b) P. Yang, J. Zhao, W. Wu, X. Yu, Y. Liu, *J. Org. Chem*., **2012**, 77, 6166-6178.